Check for updates

Amplified Madden–Julian oscillation impacts in the Pacific–North America region

Wenyu Zhou [1,5 ✉], Da Yang [1,2], Shang-Ping Xie [3] and Jing Ma [4]

The Madden–Julian Oscillation (MJO) is a slow-moving tropical mode that produces a planetary-scale envelope of convective storms. By exciting Rossby waves, the MJO creates teleconnections with far-reaching impacts on extratropical circulation and weather. Although recent studies have investigated the response of the MJO to anthropogenic warming, not much is known about potential changes in its teleconnections. Here, we show that the MJO teleconnection pattern in boreal winter will likely extend further eastward over the North Pacific. This is primarily due to an eastward shift in the exit region of the subtropical jet, to which the teleconnection pattern is anchored, and assisted by an eastward extension of the MJO itself. The eastward-extended teleconnection enables the MJO to have a greater impact downstream on the Northeast Pacific and North American west coast. Over California specifically, the multi-model mean projects a 54% increase in MJO-induced precipitation variability by 2100 under a high-emissions scenario.

The MJO[1,2] is distinct from typical equatorial waves owing to its planetary spatial scale and slow eastward propagation. The anomalous circulation and cloudiness span a horizontal scale of ~10,000 km and travel over the tropical Indian and West Pacific oceans at a speed of ~5 m s^{-1}. It usually takes more than 20 days for the large-scale convection to alternate between the enhanced and suppressed states. This enables the tropical MJO to excite quasi-stationary Rossby waves that propagate into the extratropics[3–5] and exert far-reaching impacts on regional circulation and weather[6]. The MJO teleconnection is known to affect prominent climate features, including the Pacific–North America (PNA) Pattern[7,8], North Atlantic Oscillation[9,10], stratospheric sudden warming[11,12], hurricanes[13] and monsoons[14]. Its effect on the PNA pattern, in particular, modulates blocking[15] and atmospheric rivers[16] in the Northeast Pacific, leading to profound regional impacts along the west coast of North America. The MJO is an important predictor for extended forecast beyond two weeks[17].

The MJO involves intricate interplays among wave dynamics, moist convection, radiation and air–sea coupling. Extensive studies have been devoted to investigating its physics[18–22] and numerical simulation[23–26]. The overall representation of the MJO in global climate models (GCMs) has been appreciably improved in the Coupled Model Intercomparison Project Phase 5 (CMIP5)[25] and the new CMIP6. Using selected models that properly simulate the MJO, recent studies have started to investigate future changes of the MJO[27–29]. It was found that, although the MJO precipitation and the associated convective heating will increase with enhanced vertical moisture gradient, the dynamic amplitude of the MJO, as measured by either surface wind or pressure velocity, may decrease owing to enhanced dry static stability and a more top-heavy profile of convection[30–32].

The impacts of the MJO on the extratropics depend on its teleconnection pattern, yet it is largely unexplored how the MJO teleconnection pattern will change under anthropogenic warming.

It is suspected that a weakened MJO dynamic amplitude may lead to a weakened teleconnection pattern[32], as observed in one specific model[33], but a systematic investigation is still lacking. Here, on the basis of multiple models that properly simulate the MJO, we show that future changes of the MJO teleconnection mainly manifest an eastward-extended pattern, while changes in the amplitude are uncertain. The eastward-extended teleconnection is driven by theoretically predicted large-scale changes and can be reproduced in a simple linear model. It enables the MJO to produce a larger subseasonal variability in the downstream regions, which may upset societal sectors such as agriculture, flood control and resource management.

Amplified MJO impacts from eastward-extended teleconnection

The response of the MJO teleconnection to anthropogenic warming was investigated in 11 GCMs (Supplementary Table 1), which were selected from the CMIP5 and CMIP6 archives according to their ability to properly simulate the MJO[25,34] (see Methods; Supplementary Fig. 1). The present and future warmer climates are represented by the historical (HIST) and Representative Concentration Pathway 8.5 (RCP8.5) experiments, respectively. We focus on the boreal winter (December to March), during which the MJO teleconnection in the Northern Hemisphere is most pronounced and the west coast of North America is in its rainy season. To extract the MJO-induced signals, the daily anomalous fields were band-passed (20–100 d) and composited according to the MJO phase (see Methods). The tropical state is indicated by concurrent composite of the anomalous 500 hPa pressure velocity (ω_{500}), whereas the extratropical teleconnection pattern is indicated by 6-d-lag composites of the anomalous 250 hPa geopotential height (Z_{250}), ω_{500} and precipitation. In phase 3, the tropical MJO circulation centres around the Maritime Continent and a classic PNA teleconnection pattern[35] emerges in the extratropics (Fig. 1a). The MJO–PNA pattern features strong

[1]Earth and Environmental Sciences, Lawrence Berkeley National Laboratory, Berkeley, CA, USA. [2]College of Agricultural and Environmental Sciences, University of California Davis, Davis, CA, USA. [3]Scripps Institution of Oceanography, University of California San Diego, La Jolla, CA, USA. [4]Collaborative Innovation Center on Forecast and Evaluation of Meteorological Disasters, KLME, ILCEC, Nanjing University of Information Science and Technology, Nanjing, China. [5]Present address: Atmospheric Sciences & Global Change, Pacific Northwest National Laboratory, Richland, WA, USA.
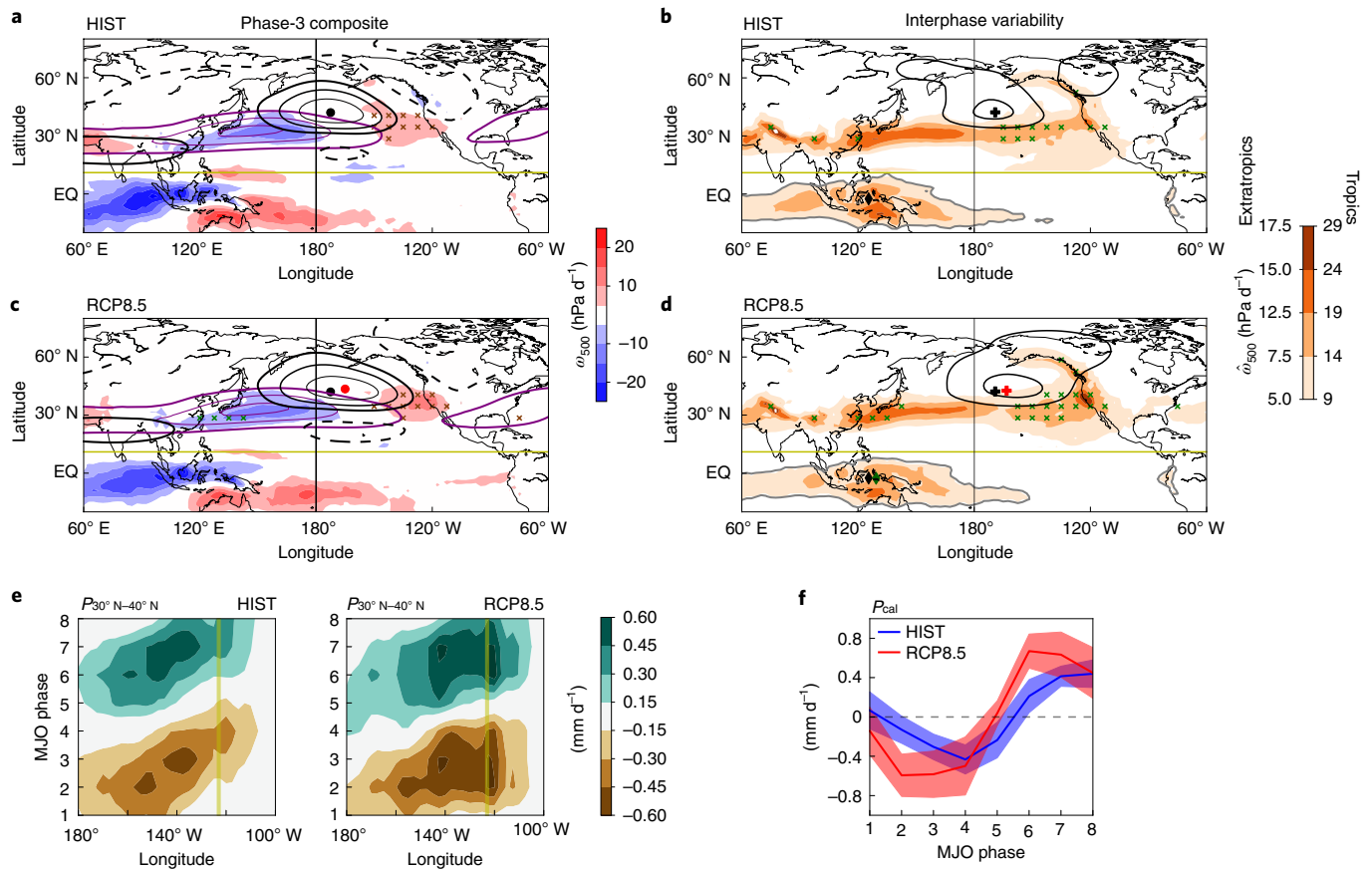✉e-mail: wenyuzhou@lbl.gov

Fig. 1 | Eastward-extended teleconnection pattern leads to amplified MJO impacts in the PNA region. a,c, Anomalous Z_{250} (contours at an interval of 12 m, solid for positive), ω_{500} (shading) and precipitation (cross symbols where the magnitude is larger than 0.35 mm d^{-1}, green for positive) associated with MJO phase 3 in HIST (**a**) and RCP8.5 (**c**). The subtropical jet, indicated by 250 hPa zonal wind ($\bar{U}_{250}$), is shown as purple contours (levels at 35 m s^{-1}, 50 m s^{-1} and 65 m s^{-1}). The dot denotes the Z_{250} centre (black for HIST and red for RCP8.5). EQ, Equator. **b,d**, MJO-induced variability in Z_{250} ($\hat{Z}_{250}$; contours at levels of 20 m and 30 m), ω_{500} ($\hat{\omega}_{500}$; shading) and precipitation (cross symbols where the magnitude is larger than 0.4 mm d^{-1}) in HIST (**b**) and RCP8.5 (**d**). The plus symbol denotes the mid-latitude $\hat{Z}_{250}$ centroid. The grey contour indicates the boundary of the active MJO region where $\hat{\omega}_{500}$ exceeds 9 hPa d^{-1}. The diamond symbol denotes the tropical $\hat{\omega}_{500}$ centroid (black for HIST and green for RCP8.5). **e**, Precipitation anomaly (P) averaged over 30° N–40° N in HIST and RCP8.5 as a function of the MJO phase and longitude. The yellow line indicates the longitude of California. **f**, Precipitation anomaly averaged over California (P_{Cal}) as a function of the MJO phase in HIST (blue) and RCP8.5 (red). The shading indicates the intermodel s.d.

Z_{250} signals near the subtropical jet exit[7,36,37] (where the westerly decelerates; $\partial \bar{U}/\partial x < 0$). This is due to barotropic energy conversion, which allows waves to effectively extract energy from the zonally asymmetric climatology[7,38,39]. The positive Z_{250} anomaly over the Northeast Pacific is associated with large-scale subsidence and drying near the west coast of North America. An opposite teleconnection pattern was found in phase 7 (Supplementary Fig. 2). In phase 1 and 5, the Rossby-wave trains are emitted from the Indian ocean and weakly affect the Northeast Pacific (Supplementary Fig. 2). Throughout the eight phases, the MJO teleconnection induces substantial Z_{250} variability that peaks near the jet exit (Fig. 1b). The associated ω_{500} and precipitation variability are strongest around 30° N and along the west coast of North America. The simulated MJO teleconnection was compared against those constructed from two reanalysis datasets (Supplementary Fig. 3). The overall patterns are similar but the simulated pattern appears to be weaker and more eastward. The eastward bias is probably related to an eastward bias in the jet exit in GCMs (Fig. 1a, Supplementary Fig. 3a).

We show that the MJO–PNA teleconnection pattern will extend further eastward under anthropogenic warming, as indicated by eastward shifts in both the centre and eastern flank of Z_{250} (Fig. 1a,c). The eastward-extended teleconnection leads to a deeper

intrusion and intensification of subsidence and drying (or ascent and wetting in phase 7) near the west coast of North America (Fig. 1a,c, Supplementary Fig. 2). A consistent eastward extension was found in phases 1 and 5 (Supplementary Fig. 2). As a result, the MJO-induced variability (measured by the s.d. across the phases) extends further eastward, with amplified variation in Z_{250} over the Northeast Pacific and in ω_{500} and precipitation along the west coast of North America (Fig. 1b,d). Focusing on the precipitation response, the Hovmöller diagram averaged over 30° N–40° N clearly illustrates that the MJO extratropical impacts extend further eastward, driving a larger precipitation variability over the downstream regions (Fig. 1e). Over California specifically, the MJO-induced precipitation variability is amplified by more than 50%, with the interphase s.d. increasing from 0.3 mm d^{-1} to 0.47 mm d^{-1} (Fig. 1f). It is also hinted that the eastward-extended teleconnection allows the MJO impacts to arrive earlier in phase in California (Fig. 1e, yellow line), leading to a forward shift in the MJO-phase-composited impacts (Fig. 1f).

In contrast to the notable eastward extension, the amplitude change of the MJO teleconnection is subtle in the multi-model mean, as measured by either the phase-composited Z_{250} peak value (Fig. 1a,c) or Z_{250} variability (Fig. 1b,d). As we discuss below,
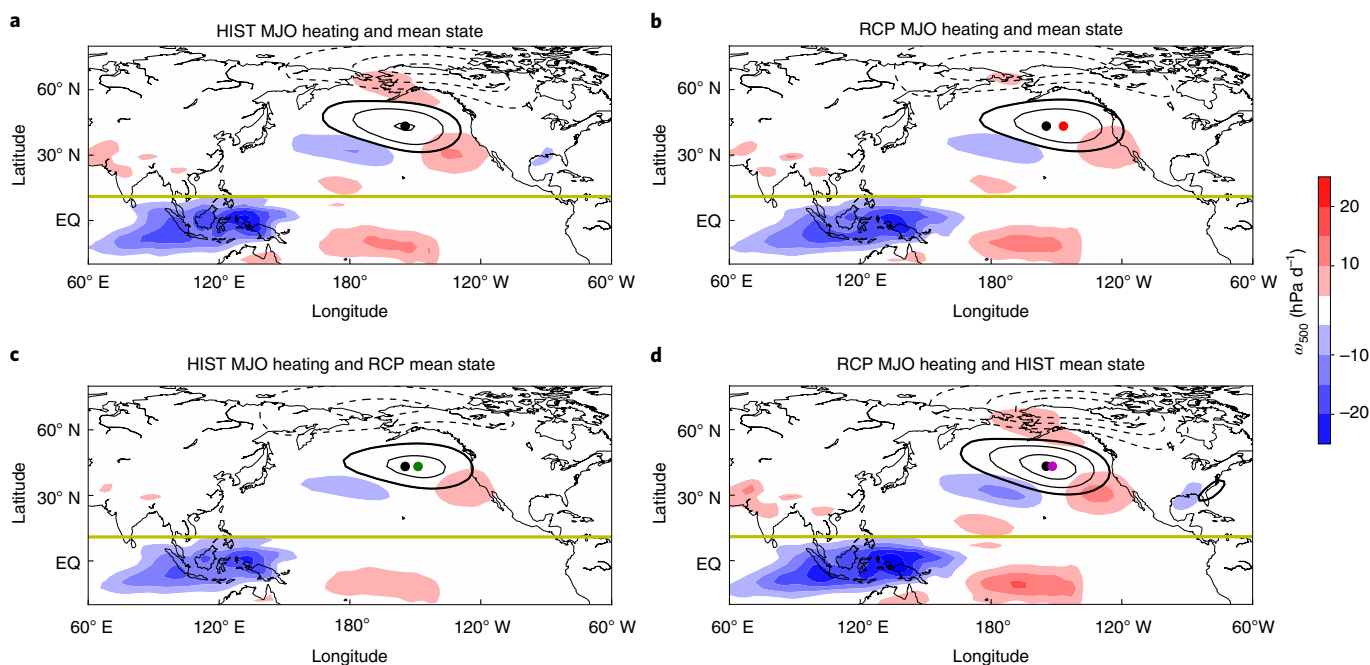
Fig. 2 | Responses of the MJO teleconnection to changes in MJO heating and large-scale mean state. a, Anomalous Z_{250} (contours at an interval of 12 m, solid for positive) and ω_{500} (shading) associated with MJO phase 3 in LBM. Both MJO heating and mean state are from HIST. **b**, Same as **a** but with MJO heating and mean state both from RCP8.5. **c**, Same as **a** but with mean state from RCP8.5. **d**, Same as **a** but with MJO heating from RCP8.5. For **a–d**, the dot symbols denote the Z_{250} centre (black for **a** and colours for **b–d**).

there is large uncertainty in the teleconnection amplitude change among models.

Causes of the eastward-extended MJO teleconnection
In light of the profound impacts of the eastward-extended MJO tele-connection, it is important to understand its causes. The MJO tele-connection pattern depends on both the tropical MJO forcing and the extratropical large-scale mean state, which modulate the source and propagation of the Rossby-wave train, respectively[34,40–42]. Under anthropogenic warming, notable changes are projected in both fac-tors. In the tropics, the MJO-phase-composited ω_{500} extends further eastward into the Central Pacific (Fig. 1a,c), and both the centroid and boundary of the MJO ω_{500} variability move eastward (Fig. 1b,d). This eastward extension of the MJO itself has been noted in pre-vious studies[32,43,44] and may drive a corresponding change in the extratropical teleconnection. In the extratropics, the subtropical jet exit is projected to shift eastward[45] (Fig. 1a,c, purple contours). The MJO teleconnection pattern, which is anchored on the jet exit through the barotropic energy conversion, may extend eastward correspondingly.

To test these hypotheses and examine their relative importance, we turned to a simple linear baroclinic model (LBM) that simulates linear responses to an eastward-propagating MJO heating in the presence of a prescribed large-scale mean state (see Methods). With imposed MJO heating and mean state calculated from the HIST simulations of GCMs, LBM reasonably captures the tropical MJO circulation and its extratropical teleconnection pattern (Fig. 2a). The Z_{250} responses peak near the jet exit region, similar to those in reanalysis and comprehensive GCMs. Under anthropogenic warm-ing, the MJO heating extends eastward and increases, whereas the mean state changes feature an eastward shift of the jet exit and a larger dry static stability (Supplementary Fig. 4). When both the MJO heating and mean state are changed to those in RCP8.5 (Fig. 2b), the teleconnection pattern extends eastward by 8° (mea-sured by shift in the Z_{250} centre) and weakens slightly. The effect

of the eastward extension dominates and leads to an ampli-fied large-scale descent near the west coast of North America. Simulations with changing mean state (Fig. 2c) or MJO heating (Fig. 2d) only were conducted to further decompose the causes. We show that the eastward-extended teleconnection is mainly driven by the jet-exit shift, which leads to a 6° teleconnection shift (Fig. 2c), and is also contributed by the eastward-extended MJO heating, which leads to a smaller 2° shift (Fig. 2d). The slightly weak-ened teleconnection amplitude reflects a net result of the opposing effects of the larger static stability (Fig. 2c) and the stronger MJO heating (Fig. 2d). Considering the bias of the climatological jet in the multi-model mean of GCMs, we have conducted additional LBM simulations with inputs from models with a good representa-tion of the climatological jet. It is confirmed that the MJO teleconnection extends eastward provided that the jet exit shifts eastward (Supplementary Fig. 5).

Drivers of MJO extension and jet-exit shift
What then drives the eastward extension of the MJO itself and the eastward shift of the subtropical jet exit? The distribution of the MJO activity is known to be sensitive to the tropical warming pattern[46]. Here we provide further evidence that the zonally asymmetric warm-ing along the Equator drives the eastward extension of the MJO. To demonstrate this point, Atmospheric Model Intercomparison Project (AMIP)-style simulations forced with uniform warming (AMIP4K) and projected patterned warming (AMIPFuture) were used (see Methods). Although these AMIP-style experiments do not consider the atmosphere–ocean coupling, their MJO propagation characteristics are similar to those of coupled models, as shown by the Hovmöller diagram of the equatorial-mean ω_{500} (Fig. 3a–c). We show that the eastward MJO extension projected in coupled mod-els (Fig. 3a) is absent in AMIP4K with uniform warming (Fig. 3b) and is reproduced only in AMIPFuture with patterned warming (Fig. 3c). The projected warming pattern features enhanced warm-ing east of the climatological warm pool (Fig. 3d), which works
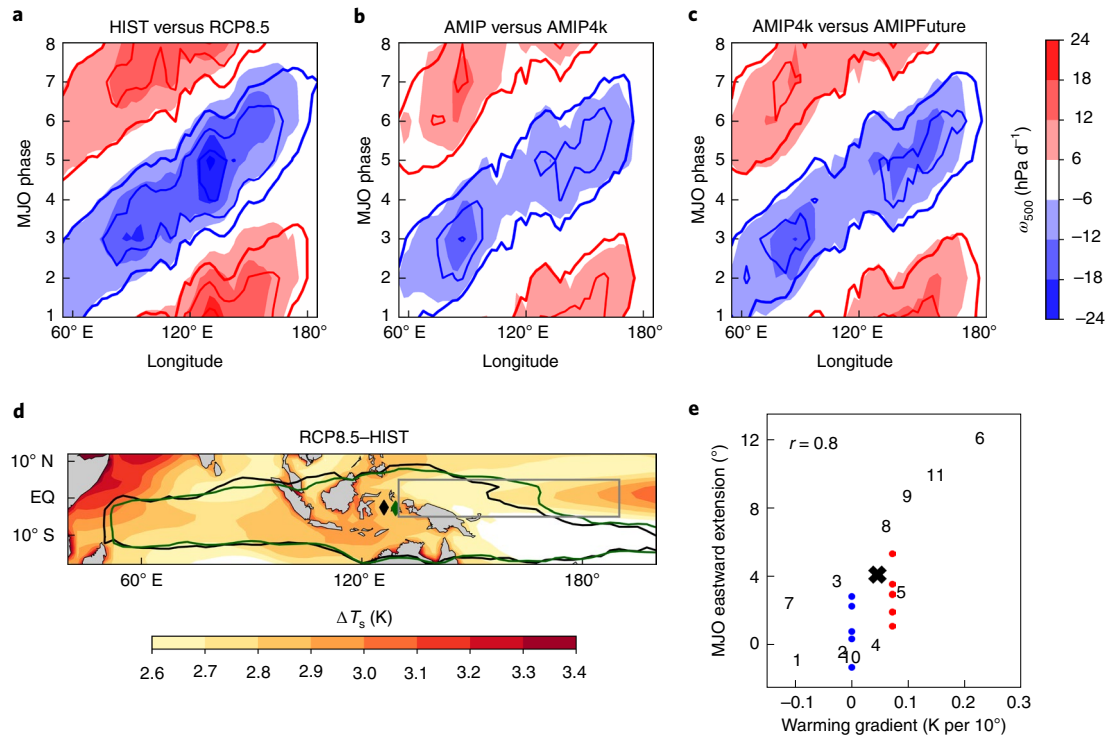
Fig. 3 | Eastward extension of the MJO itself. a, Anomalous ω_{500} averaged over 10° S–10° N as a function of the MJO phase and longitude in HIST (shading) and RCP8.5 (contours, with the same interval as in shading for HIST). **b**, Same as **a** but for AMIP (shading) and AMIP4K (contours). **c**, Same as **a** but for AMIP4K (shading) and AMIPFuture (contours). **d**, Surface warming pattern (ΔT_s) projected under anthropogenic warming by the multi-model mean. The boundary (contour) and centroid (diamond symbol) of the active MJO region are denoted (black for HIST and green for RCP8.5). **e**, Intermodel scatterplot between the warming gradient (over the longitudes denoted by the grey box in **d**) and the eastward MJO extension. Individual models are indexed and the cross symbol indicates the multi-model mean. The Pearson correlation coefficient $r = 0.8$. The blue and red dots denote the MJO extension in individual simulations of AMIP4K and AMIPFuture, respectively.

to extend the convectively unstable/moist region and, therefore, extend the MJO activity eastward (Supplementary Fig. 6). The critical role of the zonally asymmetric warming can be further observed from the intermodel spread of coupled models. Under anthropogenic warming, the more the Central Pacific is warmed compared with the West Pacific, the more the MJO extends eastward (Fig. 3e).

The exit of the subtropical jet is integrally tied to the stationary eddy pattern, which is defined as the departure in the 250 hPa geopotential height from the zonal mean (Z_{250}^*). With the strongest (weakest) jet lying south of the anomalous low (high), the jet exits near the node of Z_{250}^* (Fig. 4a). Under anthropogenic warming, the stationary eddy pattern is known to shift eastward in boreal winter[47], leading to a corresponding shift in the jet exit (Fig. 4b). Among models, the shift of the jet exit (measured by the outer contour of the subtropical jet) is highly correlated with the shift of the Z_{250}^* node (Supplementary Fig. 7a). The eastward shift of Z_{250}^* has been attributed to an increase in the stationary Rossby wavelength due to the strengthened westerlies[47] (the stationary wavelength L in linear barotropic theory[3] scales with the jet speed U as $L \propto \sqrt{U/\beta^*}$ where $\beta^* = \beta - U_{yy}$ is the meridional gradient of the absolute vorticity). The strengthened westerlies are in turn driven by the increased meridional temperature gradient due to enhanced warming in the tropical upper troposphere (Fig. 4c). This enhanced tropical upper-tropospheric warming is a direct consequence of the moist-adiabat adjustment and exists even in the AMIP-style simulation forced with uniform warming (Fig. 4c). Thus, eastward shifts of Z_{250}^* and the jet exit are consistently found from AMIP to AMIP4K (Fig. 4b), leading to a robust eastward extension of the MJO teleconnection under uniform warming (Fig. 4d).

The subtropical jet may also respond to rectification effects of the MJO changes[48] or zonal shift in the Walker circulation. However, it is improbable that these factors have a significant role in driving the eastward jet-exit shift. We note that the eastward jet-exit shift is robustly projected in models that predict opposite changes in the MJO pattern (either eastward or slightly westward; Supplementary Fig. 7b) and amplitude (either positive or negative; Supplementary Fig. 7c). The magnitude of the jet-exit shift in AMIP4K is similar to that in AMIPFuture (Fig. 4b), even though the Walker-circulation shift is projected only under patterned warming (Supplementary Fig. 8). Despite little difference in the jet-exit shift, the eastward extension of the MJO teleconnection is more pronounced in AMIPFuture than in AMIP4K (Fig. 4d). This is probably due to the contribution of the eastward extension of the MJO under patterned warming (Fig. 3c).

Robust eastward extension and uncertain amplitude change

The results above are mainly based on the multi-model mean. We now examine the results of individual models (Supplementary Figs. 9–19) and illustrate the robustness in the eastward extension of the MJO teleconnection as well as the uncertainty in the change in teleconnection amplitude. Across models, the eastward extension of the MJO teleconnection pattern (measured by the centroid of the MJO-induced Z_{250} variability) is correlated with the shift of the subtropical jet exit (Fig. 5a). Nine out of the eleven selected models (21 out of the total 25 models including those that were not selected owing to lack of good MJOs or outputs) predict an eastward shift of the subtropical jet exit. In the multi-model mean, there is a ~7°
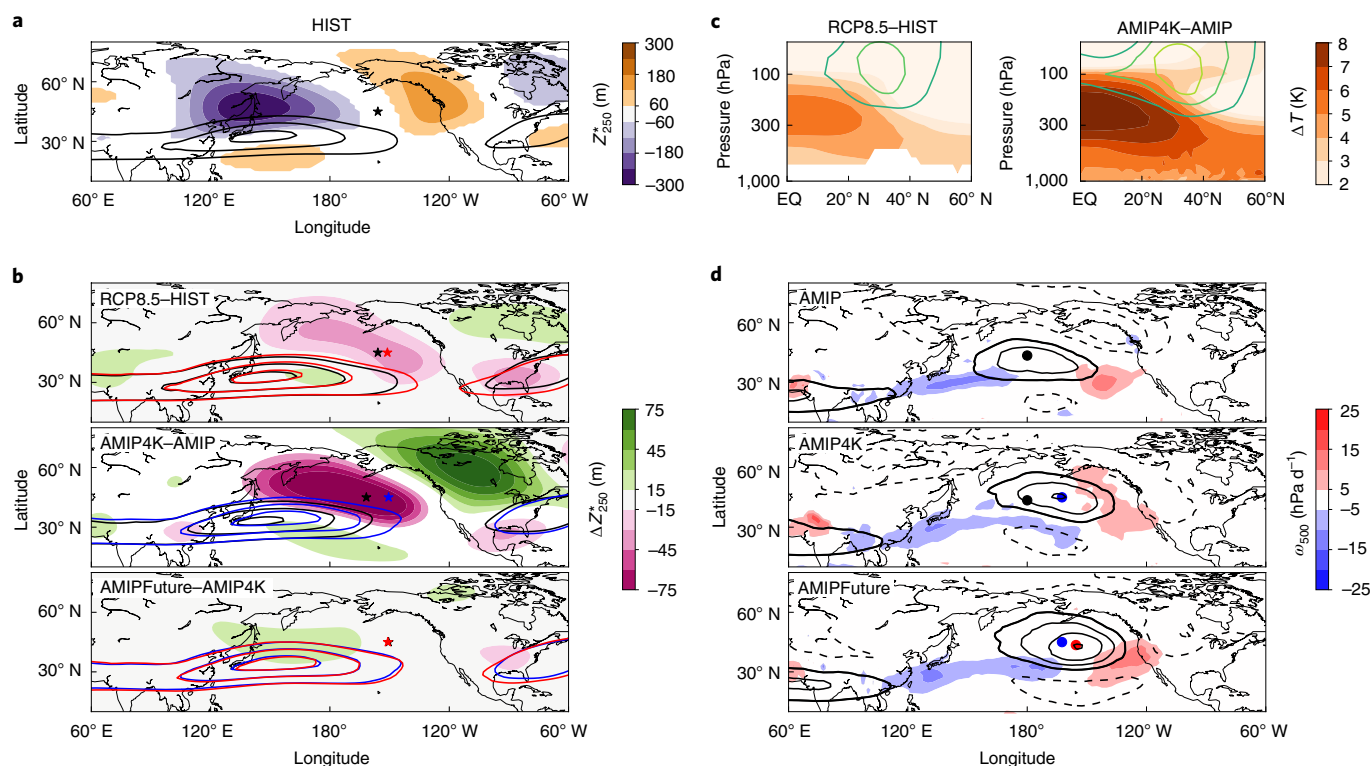
Fig. 4 | Eastward shift of the subtropical jet exit. a, Z_{250}^* (shading) and $\bar{U}_{250}$ (contours at 35 m s^{-1}, 50 m s^{-1} and 65 m s^{-1}) in HIST boreal winter. The node of Z_{250}^* is indicated by the star. **b**, Responses of Z_{250}^* (changes in shading and nodes denoted by star symbols) and $\bar{U}_{250}$ (contours) to anthropogenic warming in coupled models (top; from HIST in black to RCP8.5 in red), uniform warming (middle; from AMIP in black to AMIP4K in blue) and warming pattern (bottom; from AMIP4K in blue to AMIPFuture in red). **c**, Changes in the zonal-mean temperature (shading) and zonal wind (contours; 2.5 m s^{-1} interval) under anthropogenic warming (left; from HIST to RCP8.5) and forced by uniform surface warming (right; from AMIP to AMIP4K). **d**, MJO phase-3 teleconnection in simulations of AMIP, AMIP4K and AMIPFuture. The dots denote the Z_{250} centres (black for AMIP, blue for AMIP4K and red for AMIPFuture).

eastward shift in the jet exit and a ~7.5° eastward extension in the MJO teleconnection pattern. The eastward jet-exit shift is insensitive to the climatological bias of a more eastward jet exit in GCMs. It is robustly projected in models with both good and biased jet climatology and no correlation was found between future shift and climatological position of the jet exit (Supplementary Fig. 7d). The intermodel correlation between eastward extensions of the teleconnection pattern and the MJO itself was found to be insignificant (Fig. 5b). This is consistent with the LBM results, which show that changes in MJO heating are less effective in changing the teleconnection pattern than the jet-exit shift.

Models with a more eastward-extended MJO teleconnection exhibit a larger amplification in MJO-induced variability in California (Fig. 5c). Nine out of the eleven models predict amplified MJO impacts and the multi-model mean predicts a 35% (54%) increase in the MJO-induced ω_{500} (precipitation) variability. The larger increase in precipitation variability, compared with the variability in ω_{500}, may reflect the thermodynamic contribution from the enhanced atmospheric moisture with warming. With the high correlation between the eastward-extended teleconnection and the jet-exit shift (Fig. 5a), the amplification of the MJO impacts is further correlated with the jet-exit shift (Fig. 5d). According to the intermodel linear regression (Fig. 5d, black and red lines), a 1° eastward shift of the jet exit implies a ~5% (6%) amplification in the MJO-induced ω_{500} (precipitation) variability in California.

The MJO impacts would also be affected by changes in the amplitude of the MJO teleconnection. However, models disagree with each other on whether the MJO teleconnection amplitude will be weakened or amplified, and the multi-model mean projects little change (Fig. 5e). The amplitude change of the MJO teleconnection is not simply correlated with that of tropical MJO circulation, indicating additional influences from extratropical dynamics. The change in the teleconnection amplitude does not play a major role in explaining the intermodel spread of the changing MJO impacts in California (Fig. 5f), which is largely dominated by that of the eastward extension (Fig. 5d).

Summary and discussion
In summary, our multi-GCM diagnosis and linear dynamic model experiments reveal an eastward extension of the MJO teleconnection to the PNA region in boreal winter under anthropogenic warming. This eastward extension is mainly due to the eastward shift of the subtropical jet exit, a large-scale climate response to the global-scale warming. Furthermore, the equatorial warming pattern drives an eastward extension of tropical MJO convection and further enhances the teleconnection extension. The eastward-extended teleconnection enables the MJO to exert a larger impact in the Northeast Pacific and along the west coast of North America. Recent studies have warned of increased interannual precipitation volatility in California under anthropogenic warming[49]. The enhanced subseasonal variability illustrated here will further aggravate the situation, posing acute challenges on regional resource management and extreme weather preparation. Similar to the subseasonal MJO–PNA teleconnection, the interannual El Niño/Southern Oscillation-forced PNA pattern is also projected to extend eastward under anthropogenic warming[50]. Such robust changes in the tropical-induced PNA teleconnection arise from zonal shifts in the
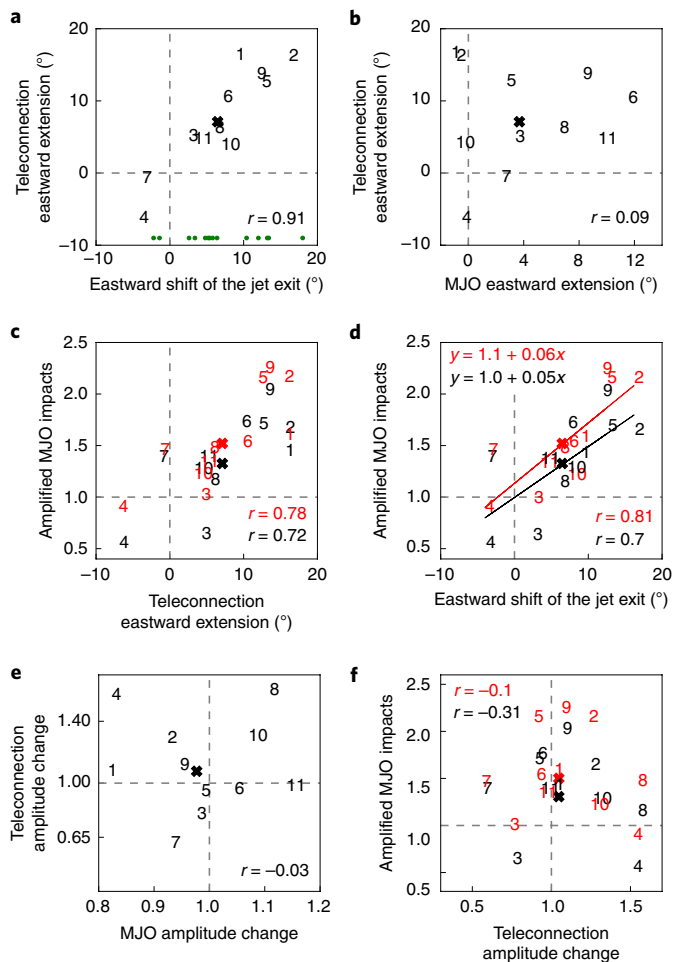
Fig. 5 | Intermodel scatterplots. a, Eastward shift of the jet exit versus eastward extension of the MJO teleconnection. The 11 selected models are indexed, whereas the 14 models that were not selected are denoted by green dots. The cross indicates the 11-model mean. **b**, Eastward extension of the MJO itself versus eastward extension of the MJO teleconnection. **c**, Eastward extension of the MJO teleconnection versus amplified MJO impacts in California (black for ω_{500}; red for precipitation). **d**, Eastward shift of the jet exit versus amplified MJO impacts in California (black for ω_{500}; red for precipitation). **e**, MJO amplitude change versus teleconnection amplitude change. **f**, Teleconnection amplitude change versus amplified MJO impacts in California (black for ω_{500}; red for precipitation). Pearson correlation coefficients r are shown. Correlation is significant at a P value of 0.05 if $r > 0.58$.

large-scale mean state and imply increased predictability beyond week 2 over winter North America.

In contrast to the notable eastward extension, the amplitude change of the MJO teleconnection is subtle in the multi-model mean and is uncertain among models. This uncertainty is not necessarily dominated by the tropical MJO forcing but can come from extratropical dynamics, such as changes in the dry static stability, zonal asymmetry of the large-scale flow and high-frequency eddy interaction. Future studies are needed to investigate the detailed mechanisms and constrain the uncertainty. Our research has focused on the PNA region, which is located downstream of the eastward teleconnection extension, and on the winter season when the MJO propagates more zonally. Further studies are needed to explore potential changes of the MJO impacts in other regions and seasons.

References

1. Madden, R. A. & Julian, P. R. Detection of a 40–50 day oscillation in the zonal wind in the tropical pacific. *J. Atmos. Sci.* **28**, 702–708 (1971).
2. Zhang, C. Madden-Julian oscillation. *Rev. Geophys.* **43**, RG2003 (2005).
3. Hoskins, B. J. & Karoly, D. J. The steady linear response of a spherical atmosphere to thermal and orographic forcing. *J. Atmos. Sci.* **38**, 1179–1196 (1981).
4. Matthews, A. J., Hoskins, B. J. & Masutani, M. The global response to tropical heating in the Madden–Julian oscillation during the northern winter. *Q. J. R. Meteorol. Soc.* **130**, 1991–2011 (2004).
5. Seo, K.-H. & Son, S.-W. The global atmospheric circulation response to tropical diabatic heating associated with the Madden–Julian oscillation during northern winter. *J. Atmos. Sci.* **69**, 79–96 (2011).
6. Zhang, C. Madden–Julian oscillation: bridging weather and climate. *Bull. Am. Meteorol. Soc.* **94**, 1849–1870 (2013).
7. Mori, M. & Watanabe, M. The growth and triggering mechanisms of the PNA: a MJO-PNA coherence. *J. Meteorol. Soc. Jpn.* **86**, 213–236 (2008).
8. Riddle, E. E. et al. The impact of the MJO on clusters of wintertime circulation anomalies over the North American region. *Clim. Dyn.* **40**, 1749–1766 (2013).
9. Cassou, C. Intraseasonal interaction between the Madden–Julian Oscillation and the North Atlantic Oscillation. *Nature* **455**, 523–527 (2008).
10. Lin, H., Brunet, G. & Derome, J. An observed connection between the North Atlantic oscillation and the Madden–Julian oscillation. *J. Clim.* **22**, 364–380 (2009).
11. Garfinkel, C. I., Feldstein, S. B., Waugh, D. W., Yoo, C. & Lee, S. Observed connection between stratospheric sudden warmings and the Madden-Julian Oscillation. *Geophys. Res. Lett.* **39**, L18807 (2012).
12. Kang, W. & Tziperman, E. The MJO-SSW teleconnection: interaction between MJO-forced waves and the midlatitude jet. *Geophys. Res. Lett.* **45**, 4400–4409 (2018).
13. Maloney, E. D. & Hartmann, D. L. Modulation of eastern North Pacific hurricanes by the Madden–Julian oscillation. *J. Clim.* **13**, 1451–1460 (2000).
14. Lorenz, D. J. & Hartmann, D. L. The effect of the MJO on the North American monsoon. *J. Clim.* **19**, 333–343 (2006).
15. Henderson, S. A., Maloney, E. D. & Barnes, E. A. The influence of the Madden–Julian oscillation on northern hemisphere winter blocking. *J. Clim.* **29**, 4597–4616 (2016).
16. Mundhenk, B. D., Barnes, E. A., Maloney, E. D. & Baggett, C. F. Skillful empirical subseasonal prediction of landfalling atmospheric river activity using the Madden–Julian oscillation and quasi-biennial oscillation. *npj Clim. Atmos. Sci.* **1**, 20177 (2018).
17. Johnson, N. C., Collins, D. C., Feldstein, S. B., L'Heureux, M. L. & Riddle, E. E. Skillful wintertime North American temperature forecasts out to 4 weeks based on the state of ENSO and the MJO. *Weath. Forecast* **29**, 23–38 (2013).
18. Raymond, D. J. & Fuchs, Ž. Moisture modes and the Madden–Julian oscillation. *J. Clim.* **22**, 3031–3046 (2009).
19. Sobel, A. & Maloney, E. Moisture modes and the eastward propagation of the MJO. *J. Atmos. Sci.* **70**, 187–192 (2012).
20. Yang, D. & Ingersoll, A. P. Triggered convection, gravity waves, and the MJO: a shallow-water model. *J. Atmos. Sci.* **70**, 2476–2486 (2013).
21. Adames, Á. F. & Kim, D. The MJO as a dispersive, convectively coupled moisture wave: theory and observations. *J. Atmos. Sci.* **73**, 913–941 (2015).
22. Khairoutdinov, M. F. & Emanuel, K. Intraseasonal variability in a cloud-permitting near-global equatorial aquaplanet model. *J. Atmos. Sci.* **75**, 4337–4355 (2018).
23. Kim, D. et al. Application of MJO simulation diagnostics to climate models. *J. Clim.* **22**, 6413–6436 (2009).
24. Jiang, X. et al. Vertical structure and physical processes of the Madden-Julian oscillation: exploring key model physics in climate simulations. *J. Geophys. Res. Atmos.* **120**, 4718–4748 (2015).
25. Ahn, M.-S. et al. MJO simulation in CMIP5 climate models: MJO skill metrics and process-oriented diagnosis. *Clim. Dyn.* **49**, 4023–4045 (2017).
26. Wang, B. et al. Dynamics-oriented diagnostics for the Madden–Julian oscillation. *J. Clim.* **31**, 3117–3135 (2018).

27. Liu, P. et al. MJO change with A1B global warming estimated by the 40-km ECHAM5. *Clim. Dyn.* **41**, 1009–1023 (2013).
28. Arnold, N. P., Branson, M., Kuang, Z., Randall, D. A. & Tziperman, E. MJO intensification with warming in the superparameterized CESM. *J. Clim.* **28**, 2706–2724 (2015).
29. Adames, Á. F., Kim, D., Sobel, A. H., Genio, A. D. & Wu, J. Changes in the structure and propagation of the MJO with increasing CO_2. *J. Adv. Model. Earth Syst.* **9**, 1251–1268 (2017).
30. Bui, H. X. & Maloney, E. D. Changes in Madden-Julian oscillation precipitation and wind variance under global warming. *Geophys. Res. Lett.* **45**, 7148–7155 (2018).
31. Bui, H. X. & Maloney, E. D. Mechanisms for global warming impacts on Madden–Julian oscillation precipitation amplitude. *J. Clim.* **32**, 6961–6975 (2019).
32. Maloney, E. D., Adames, Á. F. & Bui, H. X. Madden–Julian oscillation changes under anthropogenic warming. *Nat. Clim. Change* **9**, 26–33 (2019).
33. Wolding, B. O., Maloney, E. D., Henderson, S. & Branson, M. Climate change and the Madden-Julian oscillation: a vertically resolved weak temperature gradient analysis. *J. Adv. Model. Earth Syst.* **9**, 307–331 (2017).
34. Henderson, S. A., Maloney, E. D. & Son, S.-W. Madden–Julian oscillation pacific teleconnections: the impact of the basic state and MJO representation in general circulation models. *J. Clim.* **30**, 4567–4587 (2017).
35. Wallace, J. M. & Gutzler, D. S. Teleconnections in the geopotential height field during the Northern Hemisphere winter. *Mon. Weath. Rev.* **109**, 784–812 (1981).
36. Bao, M. & Hartmann, D. L. The response to MJO-like forcing in a nonlinear shallow-water model. *Geophys. Res. Lett.* **41**, 1322–1328 (2014).
37. Adames, Á. F. & Wallace, J. M. Three-dimensional structure and evolution of the MJO and its relation to the mean flow. *J. Atmos. Sci.* **71**, 2007–2026 (2014).
38. Simmons, A. J., Wallace, J. M. & Branstator, G. W. Barotropic wave propagation and instability, and atmospheric teleconnection patterns. *J. Atmos. Sci.* **40**, 1363–1392 (1983).
39. Ting, M. & Yu, L. Steady response to tropical heating in wavy linear and nonlinear baroclinic models. *J. Atmos. Sci.* **55**, 3565–3582 (1998).
40. Hoskins, B. J. & Ambrizzi, T. Rossby wave propagation on a realistic longitudinally varying flow. *J. Atmos. Sci.* **50**, 1661–1671 (1993).
41. Ting, M. & Sardeshmukh, P. D. Factors determining the extratropical response to equatorial diabatic heating anomalies. *J. Atmos. Sci.* **50**, 907–918 (1993).
42. Yasui, S. & Watanabe, M. Forcing processes of the summertime circumglobal teleconnection pattern in a dry AGCM. *J. Clim.* **23**, 2093–2114 (2009).
43. Subramanian, A. et al. The MJO and global warming: a study in CCSM4. *Clim. Dyn.* **42**, 2019–2031 (2014).
44. Chang, C.-W. J., Tseng, W.-L., Hsu, H.-H., Keenlyside, N. & Tsuang, B.-J. The Madden-Julian oscillation in a warmer world. *Geophys. Res. Lett.* **42**, 6034–6042 (2015).
45. Neelin, J. D., Langenbrunner, B., Meyerson, J. E., Hall, A. & Berg, N. California winter precipitation change under global warming in the coupled model intercomparison project phase 5 ensemble. *J. Clim.* **26**, 6238–6256 (2013).
46. Maloney, E. D. & Xie, S.-P. Sensitivity of tropical intraseasonal variability to the pattern of climate warming. *J. Adv. Model. Earth Syst.* **5**, 32–47 (2013).
47. Simpson, I. R., Seager, R., Ting, M. & Shaw, T. A. Causes of change in Northern Hemisphere winter meridional winds and regional hydroclimate. *Nat. Clim. Change* **6**, 65–70 (2016).
48. Kang, W. & Tziperman, E. More frequent sudden stratospheric warming events due to enhanced MJO forcing expected in a warmer climate. *J. Clim.* **30**, 8727–8743 (2017).
49. Swain, D. L., Langenbrunner, B., Neelin, J. D. & Hall, A. Increasing precipitation volatility in twenty-first-century California. *Nat. Clim. Change* **8**, 427–433 (2018).
50. Zhou, Z.-Q., Xie, S.-P., Zheng, X.-T., Liu, Q. & Wang, H. Global warming–induced changes in El Niño teleconnections over the North Pacific and North America. *J. Clim.* **27**, 9050–9064 (2014).

Methods

CMIP outputs. The HIST and RCP8.5 (RCP8.5 for CMIP5; SSP585 for CMIP6) experiments of eleven coupled GCMs were used to project changes in the MJO teleconnection under anthropogenic warming. The present and future climates were defined as HIST during 1979–2005 and RCP8.5 during 2079–2099, respectively. The eleven models were selected on the basis of their ability to simulate MJO properly. In particular, Hovmöller diagrams of MJO-phase-composited equatorial precipitation were plotted for each model, as in Fig. 4 of ref. [25]; our computations that include CMIP6 models are provided in Supplementary Figs. 9k–19k. Models that simulate reasonable MJO propagation in general have good values in the metric 'the precipitation east–west power ratio', which is computed by the Program for Climate Model Diagnosis & Intercomparison (PCMDI) and is available online (https://pcmdi.llnl.gov/pmp-preliminary-results/mjo_metrics/mjo_ewr_cmip5and6_overlap_runs_average_standalone.html). A summary of the selected models, denoted by triangles in the metric plot (Supplementary Fig. 1), is provided in Supplementary Table 1 with their names, resolutions and model centres. Eight of the models are from CMIP5 (ref. [51]) as follows: (1) CMCC-CM, (2) CNRM-CM5, (3) IPSL-CM5B-LR, (4) MIROC5, (5) MPI-ESM-LR, (6) MRI-CGCM3, (7) NorESM1-M and (8) bcc-csm1-1 (8). Three of the models are from the new CMIP6 (ref. [52]); only a few models are available now with daily outputs) as follows: (9) BCC-CSM2-MR, (10) GFDL-CM4 and (11) MRI-ESM2. The indexes in the parentheses were used to denote individual models in the scatterplots. The CESM2 and CNRM-CM6 also simulate reasonable east–west power ratio in their HIST simulations, but both of them at this time lack daily outputs of required variables for investigating future projection.

Among these 11 coupled models, 6 of them provide a complete set of AMIP, AMIP4K and AMIPFuture experiments, which were used to investigate the effects of global-scale and patterned warming on the eastward shift of the jet exit and on the eastward extension of the MJO. The six models are bcc-csm1-1, CNRM-CM5, MIROC5, MRI-CGCM3, BCC-CSM2-MR and MRI-ESM2. The AMIP simulation is forced with observed sea surface temperature (SST). In AMIP4K, a globally uniform warming of 4 K is superimposed onto the observed SST. AMIPFuture instead uses a spatially patterned warming derived from the CMIP3 1pctCO2 simulation (averaged around the time at which CO_2 is quadrupled). This warming pattern is similar to those projected in RCP8.5.

The daily-mean data were used for MJO-related diagnosis and the monthly-mean data were used to analyse the large-scale mean-state changes. For Fig. 5a and Supplementary Fig. 7, we included 14 extra models to investigate the robustness of the eastward shift in the jet exit. They are as follows: ACCESS1-0, ACCESS1-3, BNU-ESM, CCSM4, CanESM2, CESM1-CAM5, GFDL-CM3, GISS-E2-R, HadGEM2-ES, IPSL-CM5A-LR, MIROC-ESM, inmcm4, CESM2 and CNRM-CM6. All model outputs have been interpolated to a common grid of 1.5° (latitude) × 2.5° (longitude) resolution before analysis. Metrics, such as longitudes of the jet exit and Z_{250}^{*} node, were computed after further interpolating to a finer resolution of 0.2°.

Reanalysis datasets. MJO and its teleconnection are also constructed from two reanalysis datasets: NCEP-DOE[53] and ECMWF-ERA5 (ref. [54]). Daily outputs, including zonal winds, pressure velocity, geopotential height and precipitation, were used. The analysis is for boreal winter (December to March) and covers the same HIST period (1979–2005).

LBM. We used an LBM[55,56] to explain the GCM-projected eastward extension of the MJO teleconnection. LBM has been widely used in previous studies of the MJO teleconnection[33,34,57,58]. In LBM, the hydrostatic primitive equations are linearized about a mean state and the linear response to a prescribed forcing is simulated. The resolution was set to T42L20; that is, 128 × 64 grids in the horizontal and 20 sigma levels in the vertical. Horizontal diffusion with an e-folding time scale of 2 h was applied. The model also applies Newtonian damping with a time scale of 20 d for most vertical levels and a time scale of 0.5 d for the lowest and highest levels.

The model is forced by a time-evolving, eastward-propagating MJO heating (Q). We constructed this Q from the MJO-phase-composited 500 Pa pressure velocity (ω_{500}^{n}) in GCMs according to the first-order dry static energy (s) balance, that is,

$$Q \cong \omega \frac{\partial s}{\partial p}$$

First, the MJO-phase-composited heating (Q^n) was estimated from ω_{500}^n at each grid point (x, y) as

$$Q^n(x, y, \eta) = \frac{\partial s}{\partial p} \cdot \omega_{500}^n(x, y) \cdot \cos^2(\eta - 0.5)\pi$$

where n refers to the MJO phase and η is the vertical sigma level. The tropical dry static stability $\frac{\partial s}{\partial p}$ was computed from the boreal-winter climatology over the tropical Indian and West Pacific Oceans. It is $0.06\,K\,hPa^{-1}$ for HIST and $0.075\,K\,hPa^{-1}$ around the level of 500 hPa (Supplementary Fig. 4). Second, an

eastward-propagating MJO heating was constructed by interpolating Q^n at eight phases to an assumed 48 d life cycle of MJO, with 6 d for each phase. The large-scale mean state, which includes winds, temperature, geopotential height and surface pressure, was constructed from the boreal-winter climatology in GCMs. The independent effect of MJO heating and mean state was then examined by changing them from profiles in HIST to profiles in RCP8.5.

MJO-related diagnostics. The MJO life cycle is categorized into eight MJO phases, which correspond to different longitudinal locations of the enhanced convection. Following the MJO Diagnostics Package[59] provided by the US Climate Variability and Predictability (CLIVAR) MJO Working Group, we computed the MJO-phase-composited fields in the following five steps[60]: (1) Subseasonal (20–100 d) bandpass-filtered anomalies were constructed by applying a 201-point Lanczos filter to unfiltered anomalies from the climatological daily mean. (2) The first two leading empirical orthogonal functions (EOFs) of the MJO meridional pattern were generated using the equatorial-mean (10° N–10° S) subseasonal anomalies of 850 hPa zonal winds, 200 hPa zonal winds and outgoing longwave radiation (OLR). OLR was derived from NOAA satellite data and zonal winds were from the NCEP–DOE reanalysis. (3) The real-time multivariable MJO (RMM)[61] indices were computed for each selected model by projecting the simulated anomalous OLR and 250 hPa and 850 hPa zonal winds onto the reanalysis EOFs. Projection onto the reanalysis EOFs enables a consistent framework for comparison among different models. (4) The MJO phase was determined by $tan^{-1}(RMM2/RMM1)$, with each phase spanning 45° of the cycle. Phase 3 corresponds to enhanced convection over the tropical East Indian Ocean and phase 7 is characterized by enhanced convection over the tropical West Pacific. (5) Days associated with an active MJO phase were identified when the MJO amplitude ($\sqrt{RMM1^2 + RMM2^2}$) was greater than 1. Both concurrent and lag composites were obtained. The concurrent composite takes the mean of all of the days at a particular MJO phase while the X-day lag composite collects all of the days that are X-day lag of a particular MJO phase. Some of the analysis codes are adapted from the NCL scripts, which are available at https://www.ncl.ucar.edu/Applications/mjoclivar.shtml.

As described previously[34], two-tailed Student's t-tests were used to identify where the MJO-phase-composited anomaly is significantly different from zero. The d.o.f. was set for each phase as N/dM (~80), where N represents the total number of days per MJO phase and dM is the average length (in days) of the MJO phase. The Z_{250}-centre location was estimated using bootstrapping. Each time, the Z_{250}-centre location was estimated from a subsample (1/8 of the total MJO days for a particular phase) mean, and this was repeated 2,000 times. These statistical analyses have been applied to each model (Supplementary Figs. 9–19).

Metrics. The MJO-induced variability is defined as the s.d. of the MJO-phase-composited anomaly across the eight MJO phases. The eastward extension of the MJO itself is measured by the eastward shift in the longitudinal centroid (θ_ω) of the tropical MJO ω_{500} variability ($\hat{\omega}_{500}$). θ_ω is defined as

$$\theta_\omega = \frac{\int_{60° E}^{150° W} \int_{12° S}^{8° N} \hat{\omega}_{500}^{+} d\phi \, \theta d\theta}{\int_{60° E}^{150° W} \int_{12° S}^{8° N} \hat{\omega}_{500}^{+} d\phi \, d\theta}$$

where ϕ is the latitude and θ is the longitude. $\hat{\omega}_{500}^{+}$ refers to $\hat{\omega}_{500}$ that is larger than the tropical (12° S to 8° N) mean $\hat{\omega}_{500}$. Smaller $\hat{\omega}_{500}$ is omitted in the computation to emphasize the MJO active region.

The eastward extension of the MJO teleconnection is measured by the eastward shift in the longitudinal centroid ($\theta_{\hat{z}}$) of the MJO-induced Z_{250} variability ($\hat{Z}_{250}$) in the mid-latitudes. $\theta_{\hat{z}}$ is defined as

$$\theta_{\hat{z}} = \frac{\int_{130° E}^{130° W} \int_{30° N}^{50° N} \hat{Z}_{250}^{+} d\phi \, \theta d\theta}{\int_{130° E}^{130° W} \int_{30° N}^{50° N} \hat{Z}_{250}^{+} d\phi \, d\theta}$$

$\hat{Z}_{250}^{+}$ refers to $\hat{Z}_{250}$ that is larger than three times the mid-latitude (30° N to 50° N) mean $\hat{Z}_{250}$. Smaller $\hat{Z}_{250}$ is omitted in the computation to emphasize the centre of the MJO teleconnection pattern.

The eastward shift of the stationary eddy pattern is measured by the eastward shift in the node of Z_{250}^{*}, defined as the zero-crossing point of the mean Z_{250}^{*} averaged from 40° N–50° N. The longitude of the subtropical jet exit is defined as where the mean jet speed (averaged over 27° N–45° N where the jet peaks) falls below $40\,m\,s^{-1}$. The enhanced warming east of the climatological warming pool is measured by the longitudinal gradient in the equatorial (5° S–5° N) surface warming from 130° E to 170° W.

The amplitude of the MJO extratropical teleconnection is measured as the average of the Z_{250} peak values associated with phase 3 and 7. We choose not to include phases 1 and 5 because, in some GCMs, their teleconnection patterns do not present a clear Z_{250} peak over the North Pacific. The amplitude of tropical MJO circulation is measured as the area mean (12° S to 8° N, 60° E to 150° W) of the MJO ω_{500} variability.

References

51. Taylor, K. E., Stouffer, R. J. & Meehl, G. A. An overview of CMIP5 and the experiment design. *Bull. Am. Meteorol. Soc.* **93**, 485–498 (2011).
52. Eyring, V. et al. Overview of the coupled model intercomparison project phase 6 (CMIP6) experimental design and organization. *Geosci. Model Dev.* **9**, 1937–1958 (2016).
53. Kanamitsu, M. et al. NCEP–DOE AMIP-II Reanalysis (R-2). *Bull. Am. Meteorol. Soc.* **83**, 1631–1644 (2002).
54. *ERA5: Fifth Generation Of ECMWF Atmospheric Reanalyses Of The Global Climate* (Copernicus Climate Change Service, acessed April 2019); https://doi.org/10.5065/D6X34W69
55. Watanabe, M. & Kimoto, M. Atmosphere-ocean thermal coupling in the North Atlantic: a positive feedback. *Q. J. R. Meteorol. Soc.* **126**, 3343–3369 (2000).
56. Watanabe, M. & Jin, F.-F. A moist linear baroclinic model: coupled dynamical–convective response to El Niño. *J. Clim.* **16**, 1121–1139 (2003).
57. Lee, H.-J. & Seo, K.-H. Impact of the Madden-Julian oscillation on Antarctic sea ice and its dynamical mechanism. *Sci. Rep.* **9**, 10761 (2019).
58. Shao, X., Li, S., Liu, N. & Song, J. The Madden–Julian oscillation during the 2016 summer and its possible impact on rainfall in China. *Int. J. Climatol.* **38**, 2575–2589 (2018).
59. CLIVAR Madden–Julian Working Group MJO simulation diagnostics. *J. Clim.* **22**, 3006–3030 (2009).
60. Zhou, W. Code for MJO-related analyses and preparing input for LBM simulations. *Zenodo* https://doi.org/10.5281/zenodo.3746868 (2020).
61. Wheeler, M. C. & Hendon, H. H. An all-season real-time multivariate MJO index: development of an index for monitoring and prediction. *Mon. Weath. Rev.* **132**, 1917–1932 (2004).